

# The Gaseous Electronics Conference radio-frequency reference cell: A defined parallel-plate radio-frequency system for experimental and theoretical studies of plasma-processing discharges

P. J. Hargis, Jr., K. E. Greenberg, P. A. Miller, J. B. Gerardo, J. R. Torczynski,  
M. E. Riley, and G. A. Hebner  
*Sandia National Laboratories, Albuquerque, New Mexico 87185*

J. R. Roberts, J. K. Olthoff, J. R. Whetstone, R. J. Van Brunt, and M. A. Sobolewski  
*National Institute of Standards and Technology, Gaithersburg, Maryland 20899*

H. M. Anderson, M. P. Splichal, and J. L. Mock  
*Department of Chemical and Nuclear Engineering, University of New Mexico, Albuquerque,  
New Mexico 87131*

P. Bletzinger and A. Garscadden  
*Wright Laboratory, Wright Patterson Air Force Base, Ohio 45433*

R. A. Gottscho  
*AT&T Bell Laboratories, Murray Hill, New Jersey 07974*

G. Selwyn, M. Dalvie, and J. E. Heidenreich  
*IBM T. J. Watson Research Center, Yorktown Heights, New York 10598*

Jeffery W. Butterbaugh  
*IBM General Technology Division, Essex Junction, Vermont 05452*

M. L. Brake, M. L. Passow, J. Pender, and A. Lujan  
*Department of Nuclear Engineering, University of Michigan, Ann Arbor, Michigan 48109*

M. E. Elta  
*Department of Electrical Engineering, University of Michigan, Ann Arbor, Michigan 48109*

D. B. Graves  
*Department of Chemical Engineering, University of California, Berkeley, California 94720*

H. H. Sawin  
*Department of Chemical Engineering, MIT, Cambridge, Massachusetts 02139*

M. J. Kushner and J. T. Verdeyen  
*Department of Electrical Engineering, University of Illinois, Urbana, Illinois 61801*

R. Horwath and T. R. Turner  
*SEMATECH, Austin, Texas 78741*

(Received 14 December 1992; accepted for publication 3 September 1993)

A "reference cell" for generating radio-frequency (rf) glow discharges in gases at a frequency of 13.56 MHz is described. The reference cell provides an experimental platform for comparing plasma measurements carried out in a common reactor geometry by different experimental groups, thereby enhancing the transfer of knowledge and insight gained in rf discharge studies. The results of performing ostensibly identical measurements on six of these cells in five different laboratories are analyzed and discussed. Measurements were made of plasma voltage and current characteristics for discharges in pure argon at specified values of applied voltages, gas pressures, and gas flow rates. Data are presented on relevant electrical quantities derived from Fourier analysis of the voltage and current wave forms. Amplitudes, phase shifts, self-bias voltages, and power dissipation were measured. Each of the cells was characterized in terms of its measured internal reactive components. Comparing results from different cells provides an indication of the degree of precision needed to define the electrical configuration and operating parameters in order to achieve identical performance at various laboratories. The results show, for example, that the external circuit, including the reactive components of the rf power source, can significantly influence the discharge. Results obtained in reference cells with identical rf power sources demonstrate that considerable progress has been made in developing a phenomenological understanding of the conditions needed to obtain reproducible discharge conditions in independent reference cells.

## I. INTRODUCTION

Results of electrical measurements made on radio-frequency (rf) glow discharge systems are affected by the configuration of the electrodes and the chamber, materials of construction, external power circuitry, internal electrical power connections, means of coupling between the rf generator and electrodes, location of diagnostic probes, and various other parameters such as surface conditioning, gas impurities, and plasma instabilities. Moreover, there is a strong coupling between the external circuit and the discharge, such that the characteristics of the discharge are affected by the internal impedance of the power source as well as the components employed to couple the source to the plasma. While the basic effects of these variables are generally acknowledged, there has been little systematic research to determine their influence on the discharge. The presence of so many interrelated parameters that vary from apparatus to apparatus makes it difficult to isolate the processes which cause the plasma to vary from experiment to experiment, thereby making it difficult to compare results in a meaningful way. Because of this, there has been considerable debate about the set of operating parameters and the precision that the measurements must have to replicate experiments at different laboratories. Of a more practical concern, the lack of a full understanding of the effects of these variables upon plasma conditions has impeded our understanding of why seemingly identical commercial plasma-etching reactors often produce quite different etching results.

It has been suggested that using several identical rf research plasma chambers to perform similar experiments could aid in isolating the effects of cell geometry from some of the other variables mentioned above. By equipping similar chambers with a wide variety of diagnostic tools, a comparison of measurements made by different research groups would allow one to assess the extent to which an rf plasma discharge can be reliably reproduced. In addition, many detailed studies of discharges in a commonly used chamber design may provide information concerning unquantified plasma parameters (such as surface charging).

With these points in mind, the concept for a reference rf plasma chamber was developed at the 1988 Gaseous Electronics Conference (GEC). The basic purpose of the reference chamber (or reference cell) is to provide an experimental platform for the comparison of plasma measurements made on a common chamber geometry by different research groups. Through these measurements we hope to establish necessary and sufficient conditions to define reproducible plasma parameters and to establish a reference rf-excited plasma that permits one to define and calibrate diagnostic measurements and theoretical models of plasma processing. Initial measurements have addressed the basic voltage and current properties of the discharge. As more experience is gained with the reference cell, measurement techniques will be developed to characterize other discharge parameters, e.g., optical emission, electron density, etc. The existence of a large number of independent measurements on a single chamber design are expected to encourage theoretical studies of the detailed

plasma processes within the reference cell, thus facilitating the comparison of results between theory and experiment and between theories. The reference cell results should also provide guidance to those who intend to conduct research on rf plasmas but who are not experts in rf-related measurements. It should be pointed out that the design of the reference cell is a compromise to produce a relatively simple chamber which can be used to simulate commercial parallel-plate plasma-etching reactors. Other designs, both simpler or more complex, could be designated as "reference cells" when subjected to tests similar to those discussed in this article.

The initial voltage and current measurements were carried out in six chambers of identical design, five of which were fabricated by a single manufacturer. The chambers were located at five laboratories that agreed to participate in the initial Reference Cell Project: National Institute of Standards and Technology (NIST), Sandia National Laboratories (SNL), University of Michigan (UMI), University of New Mexico (UNM), and Wright Laboratory (WRL). Ostensibly identical measurements were made at the different laboratories and the results were compared.

Since power is the single parameter most often used to characterize a plasma reactor while voltage and current represent basic parameters of discharge operation, each laboratory measured voltage and current wave forms. From these measurements, the amplitudes and relative phases of the Fourier components of the wave forms, the self-bias voltage (dc bias), and the dissipated power were then calculated for comparison.

Before discussing the voltage and current properties of discharges in the reference cell, we summarize the reference cell design in Sec. II and in Sec. III discuss equivalent-circuit models used to calculate voltage and current values at the powered electrode from the measured values. Results from the different laboratories are then compared in Sec. IV. From these comparisons, the effect of the driving circuit, differing rf power supplies, voltage and current measurement probes, matching networks, and electrode insulators have become evident. Finally, it should be noted that the data in this article correct errors in previous unpublished reports.<sup>1,2</sup>

## II. GEC RF REFERENCE CELL

### A. Development

An *ad hoc* committee formed at the 1988 Gaseous Electronics Conference developed a preliminary design for a reference cell based on four guidelines:

- (1) ease of duplication,
- (2) compatibility with a wide variety of diagnostic measurements,
- (3) compatibility with the reactive gases used in plasma processing, and
- (4) relevance to discharge geometries used in the manufacture of semiconductor devices.

The reference cell design was finalized in March 1989, and

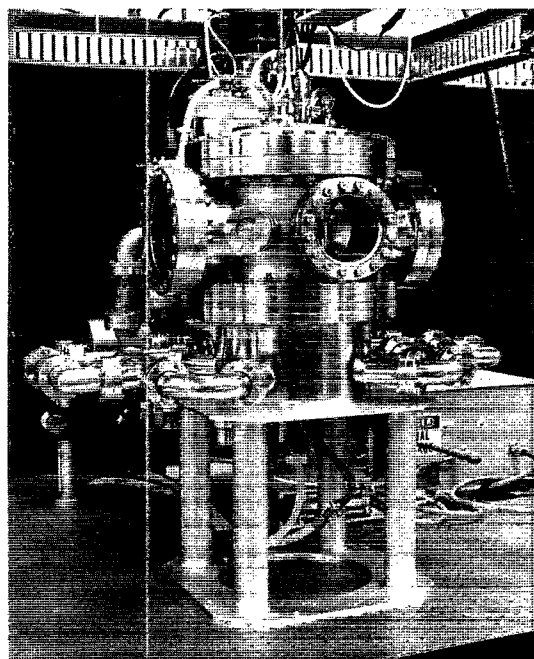


FIG. 1. Photograph of the GEC rf reference cell.

six chambers were built to test the reference cell concept. Engineering drawings for the reference cell were developed and are available to interested research groups and equipment manufacturers.<sup>3</sup>

## B. Design

The reference cell consists of a stainless-steel chamber with parallel-plate electrodes having a diameter of 102 mm. Conventional ultrahigh vacuum (UHV) sealing technology is used for all ports and flanges on the chamber and O-rings are used to seal the electrode insulators. A photograph of the reference cell is shown in Fig. 1. In the standard reference cell configuration, the interelectrode spacing is fixed at 25.4 mm. Gas is injected into the discharge region through the upper electrode and is pumped out through the manifold shown in Fig. 2. Optional hardware has been designed for mass-spectrometer sampling through the lower electrode and for a movable electrode configuration which allows continuous adjustment of the interelectrode spacing from 12.7 to 63.5 mm. (Neither of these provisions has been implemented on the existing reference cells.) Each electrode is isolated from the chamber by an electrical insulator so that the individual electrodes can be powered, grounded, biased, or allowed to float. Ground shields surround the insulators and extend from the electrode mounting flange to the plane of the electrode. The ground shields reduce sputtering of the insulator material and help to improve the uniformity of the electric field between the parallel-plate electrodes.

Eight ports are arranged around the main chamber to provide easy access to the discharge region for diagnostic measurements. Four of these are  $2\frac{1}{2}$  in. ports. Two 8 in. ports provide optical access to the entire discharge region

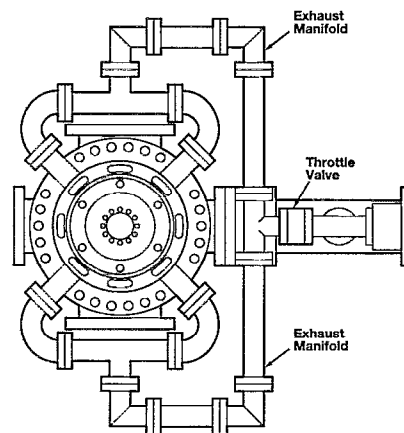


FIG. 2. Schematic diagram of the pump-out manifold for the GEC rf reference cell.

between the parallel-plate electrodes. Two 6 in. ports are also provided, with one used for connecting a turbomolecular pump to achieve the desired base pressure.

The reference cell was designed to achieve a base pressure in the range of  $10^{-5}$  Pa with a 300  $\ell/s$  turbomolecular pump and to operate at a maximum pressure of about 1300 Pa. The gas inlet, incorporated in the top electrode, has 169 equally spaced holes (305  $\mu\text{m}$  diam) placed on concentric circles in a "showerhead" pattern. Gas, injected into the discharge region through the electrode, flows through the main chamber into a pump-out chamber through a series of annular slots in the lower flange. The pump-out manifold configuration (illustrated in Fig. 2) was developed to reduce azimuthal variations in the flow characteristics of the chamber at pressures above 13 Pa. Calculations showed that relatively large azimuthal variations occur when one pump-out port is used; whereas, with four ports, as used in the reference cell configuration, the variation is reduced to approximately 10%. It is particularly important to minimize azimuthal variations in the gas pumping speed when chemically reactive gases are used, as variations in the pumping speed affect the gas residence time and hence the discharge chemistry.

Calculations of the chamber's flow characteristics for a mass flow rate of 100 sccm He (sccm denotes cubic centimeters per minute at STP) at a pressure of 13 Pa using the fluid dynamics code FIDAP (Fluid Dynamics International, Inc.) have shown regions of recirculating flow in various corners of the chamber. The flow streamlines in these areas are closed loops. Gas can be expected to have substantially longer residence times in these areas under steady state conditions. Reduced gas conductance through the pump-out manifold restricts the chamber pumping speed at low operating pressures. With a 300  $\ell/s$  turbomolecular pump, argon gas pressures less than 6.7 Pa can only be achieved at flow rates less than 10 sccm. To operate at lower pressures, one can bypass the pump-out manifold and pump directly through one of the 6 or 8 in. ports. At such pressures, the gas flow is more diffusive and azimuthal variations in the gas residence time will be mini-

mized. This or similar schemes have been implemented on most chambers.

### III. ELECTRICAL CHARACTERIZATION

#### A. Goals

A major focus of early discussions about the reference cell was the definition of a diagnostic tool set to determine when two cells were operating in a similar manner. It was decided that measurements of voltage and current wave forms (including the dc bias) should be made by all groups as cells operating with identical voltage and current wave forms in identical gases should have quite similar plasma characteristics. The goal was to apply a set of specified peak-to-peak voltages to the discharge (capacitively coupled) and to record the resulting wave forms. The data would consist of the amplitudes and phases of the first five Fourier components (harmonics) of voltage and current, along with the values of dc bias. (In this article, the component at the drive frequency  $\omega$  is referred to as the fundamental or first harmonic component. Higher-frequency components at frequency multiples  $n\omega$  are referred to as  $n$ th harmonic components.) These data sets would be gathered over a specified range of pressures. The cell was to be driven asymmetrically, with one electrode powered and the other grounded.

Ultra-high-purity (99.999% or better) argon, at a flow rate of 20 sccm, was selected for the voltage and current measurements. There were a number of reasons why an inert gas was chosen even though a major purpose of the reference cell is to study discharges in reactive gases. First, an inert gas would provide a more controlled experiment for comparing the characteristics of different reference cells. Second, an inert gas would serve as a benchmark for the behavior of a "clean" cell. (After using the cell with wafers and reactive gases, it would then be possible to determine if contamination affected the operation of the discharge. Cleaning techniques could be tested to establish a procedure for recovering the original "clean"-cell behavior.) Finally, the data could be used to help validate theoretical models of the rf discharge. The plasma chemistry of inert gases is simplified and more fundamental data (cross sections, etc.) are available for these gases. Therefore, modeling a cell using inert gases should be less subject to questions regarding gas phase chemistry and cross section data sets.

#### B. Measurement issues

In principle, voltage and current measurements are straightforward. In practice, there were several difficulties associated with rf shielding and grounding.<sup>4</sup> Improper shielding and grounding were manifested in a variety of ways including fluctuating oscilloscope wave forms, discharge instabilities, and coupling of the rf into the circuitry of other nearby equipment.

The desire to accurately measure phase as well as amplitude at frequencies from 13.56 to 67.80 MHz (5th harmonic) required investigating the accuracy of the voltage and current probes and developing proper procedures for

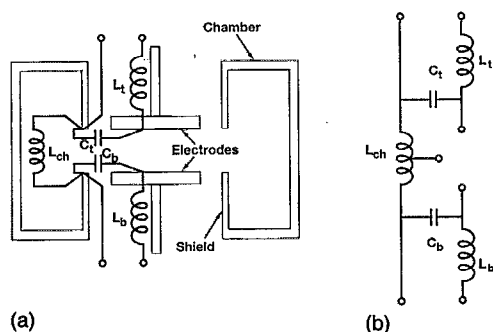


FIG. 3. Schematic diagram of the reference cell showing (a) the origin of the equivalent-circuit parameters. The subscripts "t" and "b" denote top and bottom; the two sides of the cell may have different circuit parameters in some cases. The redrawn circuit diagram (b) shows the circuit more clearly.

calibration and phase correction. It was felt that a measurement accuracy of roughly 10% or better would be sufficient to identify any major problems in plasma generation or diagnostic procedures that might occur in initial tests. Amplitude and phase errors above the 10% level were known to be present at high harmonic frequencies in some voltage and current probes. While the probe errors tend to become large at high frequencies, there often is little signal amplitude at the 4th and 5th harmonic components of the voltage and current wave forms.<sup>5</sup> Capacitive voltage probes and inductive current probes (see Sec. III F) were suggested as one way to obtain excellent amplitude and phase response at high frequency. However, most of the research groups have used commercial probes for the initial measurements.

The voltage and current at the powered electrode can be quite different from the voltage and current at the point of measurement (position where the probes are physically located). This is primarily due to inductance between the measurement point and the electrode and capacitance between the electrode and the ground shield. Problems in fabricating alumina insulators for the first set of reference cells led to two types of cells, those with alumina insulators and those with PTFE (Teflon<sup>®</sup>) insulators. Due to the different dielectric constants for alumina and PTFE and differences in the techniques used to make electrical connections to the electrodes, a comparison of external voltage and current values measured in different cells would not be meaningful. This led to the development of equivalent-circuit models that could be used to calculate voltage and current at the powered electrode from voltage and current measured at some point located away from the electrode.

#### C. Equivalent electrical circuit

The origin of the reference cell circuit parameters is shown in Fig. 3(a). An equivalent electrical circuit based on Fig. 3(a) is shown in Fig. 3(b). The circuit contains three inductances and two capacitances and includes several possible current paths between the plasma and cell components. The model omits resistive losses, interelectrode capacitance, and the input capacitance associated with the measurement circuitry, e.g., voltage-probe capac-

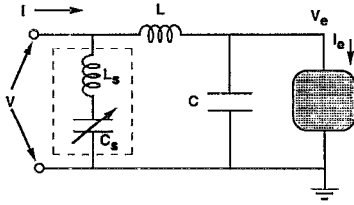


FIG. 4. Simplified  $L$ - $C$  equivalent circuit representing the reference cell. (Note that the simplified circuit does not include the shunt circuit.)  $I_e$  denotes all currents leaving the powered electrode. Those currents might flow to any of the other parts of the cell indicated in Fig. 3. With the added shunt circuit, the equivalent circuit includes the components enclosed by the dotted box.  $C_s$  is used to tune the  $L_s$ - $C_s$  shunt to eliminate (subtract) the displacement current at 13.56 MHz from the measured current. The result is that the measured current  $I_1$  is proportional to the electrode current  $I_{e1}$  with the constant of proportionality being a real number approximately equal to one for typical reference cell parameters.

itance. Even in this simplified form, this model could not be used to analyze the initial voltage and current data because measurements were not available of the current flow through all the various possible paths internal to the cell. Also, there were no simple techniques to reliably determine component values for the circuit model at all the participating laboratories.

The circuit in Fig. 3(b) was simplified to obtain the  $L$ - $C$  (inductance-capacitance) circuit shown in Fig. 4. The circuit consists of a single series inductance  $L$ , between the measurement point and the powered electrode, and a shunt capacitance  $C$ , from the powered electrode to ground. If the lower electrode is powered, the inductor represents the inductance ( $L_b$  in Fig. 3) of the power input lead between the measurement point and the powered electrode while the capacitor represents primarily the capacitance ( $C_b$  in Fig. 3) between the electrode and the surrounding ground shield. The circuit applies for an asymmetrically driven system. In the analysis below, a prescription is given for relating the interior voltage (from the powered electrode to the nearest ground shield) and current entering the plasma to the values measured at the access terminals. In this article, voltage and current values at the powered electrode are referred to as the "electrode" voltage and current, respectively. The electrode voltage and current are the parameters used to compare cells at each laboratory. While the current leaving the powered electrode (i.e., the electrode current) is the plasma current, the plasma voltage differs from the electrode voltage by the voltage drop across a lumped reactance composed of the chamber inductance ( $L_{ch}$  in Fig. 3) and the other (grounded) electrode's circuitry ( $L_t$  and  $C_t$  in Fig. 3). Even though the circuit in Fig. 4 is an approximation, it is believed to be adequate to determine if cells at different laboratories are operating in a similar manner. Improvements to the equivalent-circuit treatment are being developed.<sup>6</sup>

## D. Electrode voltage and current

Analysis of the circuit in Fig. 4 shows that the  $n$ th harmonic components of the complex electrode voltage  $V_{en}$

and current  $I_{en}$  are related to the  $n$ th harmonic components of the measured complex voltage  $V_n$  and current  $I_n$  by

$$V_{en} = V_n - j\omega_n L I_n \quad (1)$$

and

$$I_{en} = (1 - \omega_n^2 LC) I_n - j\omega_n C V_n, \quad (2)$$

where the subscript  $n$  refers to the  $n$ th harmonic,  $\omega_n = n\omega$ , and  $\omega$  is the angular frequency at the fundamental driving frequency ( $\omega = 2\pi \cdot 13.56 \times 10^6$  rad/s).

A problem with applying Eqs. (1) and (2) is that, for actual cell parameters, the electrode current can be small compared to the measured current. (This situation also occurs with many other research and commercial discharge cells.<sup>7-9</sup>) Most of the measured current is a displacement current,  $j\omega_n C V_{en}$ , due to the capacitance between the electrode and the ground shield. The displacement current is not the quantity of interest. Thus, one can be faced with finding the difference between two large numbers (measured current minus the displacement current). Consequently, calculating the electrode current is quite sensitive to errors in measuring  $V_n$  and  $I_n$ , and to errors in measuring the circuit parameters  $L$  and  $C$ . To avoid this difficulty, an external inductive reactance was added in parallel with the cell, between the power input line and ground. The purpose of the external shunt inductance is to cancel the cell's capacitive reactance at 13.56 MHz, and thereby eliminate large displacement currents from the measurement circuit. The external shunt circuit, surrounded by the dotted box in Fig. 4, consists of a fixed inductor  $L_s$  and a variable capacitor  $C_s$ . The capacitor is present for ease in tuning the shunt and to maintain capacitive coupling to the cell.

To tune the shunt circuit, the empty cell ( $10^{-5}$  Pa) is excited with a low voltage sinusoid at 13.56 MHz, and the shunt capacitor  $C_s$  is adjusted until the measured current is nulled. At this point, the net reactance,  $j\omega L_s + 1/(j\omega C_s)$ , of the shunt cancels the net reactance,  $j\omega L + 1/(j\omega C)$ , of the cell's equivalent circuit

$$j\omega L_s + 1/(j\omega C_s) = -[j\omega L + 1/(j\omega C)]. \quad (3)$$

When the shunt circuit is employed, the equations relating  $V_{en}$  and  $I_{en}$  to the measured  $V_n$  and  $I_n$  are

$$V_{en} = V_n - j\omega_n L I_{sn} \quad (4)$$

and

$$I_{en} = (1 - \omega_n^2 LC) I_{sn} - j\omega_n C V_n, \quad (5)$$

where  $I_{sn}$  is given by

$$I_{sn} = I_n - j\omega_n C_s V_n / (1 - \omega_n^2 L_s C_s). \quad (6)$$

In general, Eqs. (4)–(6) are more complicated than Eqs. (1) and (2). However, at the frequency at which the circuit was nulled, a key simplification results. This is seen by substituting Eq. (3) into Eqs. (4)–(6), obtaining

$$I_{e1} = (1 - \omega^2 LC) I_1. \quad (7)$$

Thus,  $I_{e1}$  and  $I_1$  are related by a real constant (no phase shift), which for typical cell parameters is approximately equal to 1. That is, the measured fundamental current is almost equal to the electrode (or plasma) current.

The dissipated power  $P$  is calculated from  $V_{en}$  and  $I_{en}$  using the expression

$$P = 1/2 \sum_{n=1}^{n=5} V_{en} I_{en} \cos \phi_{en}, \quad (8)$$

where  $\phi_{en}$  is the phase of  $V_{en}$  relative to  $I_{en}$ , and  $V_{en}$  and  $I_{en}$  are the magnitudes of  $V_{en}$  and  $I_{en}$ , respectively. Although the power is computed using the first five harmonics, the data in Sec. IV show that the primary contribution is that of the fundamental frequency component. Equation (8) is used to calculate the dissipated power whether or not the shunt circuit is used.

The shunt circuit has been tested successfully at many laboratories. However, its use requires further consideration. The cell and the shunt are not pure reactances but also contain resistive losses. Therefore, the shunt does not exactly null the measured current; some residual current is present even with the shunt properly tuned. Typically, the residual measured current is 0.5% of the current without the shunt present. Measurement of this residual current can be used to determine the quality factor  $Q$  of the cell-shunt circuit and its equivalent series resistance. One of the reference cells which used AWG-#10 wire for the shunt coil had a  $Q$  of 216 (at 13.56 MHz) and an equivalent series resistance  $R_s = 0.94 \Omega$ . This resistance can introduce errors because it is not included in the circuit model. If the shunt circuit has been tuned to resonance with the cell at the fundamental frequency, the current magnitude  $I_r$ , circulating through the resistance is approximately

$$I_r = \omega CV / (1 - \omega^2 LC), \quad (9)$$

where  $V$  is one-half the peak-to-peak driving voltage. This expression applies whether or not a discharge is present. The power  $P_r$  dissipated in the resistance is

$$P_r = I_r^2 R_s / 2 = R_s (\omega CV)^2 / (1 - \omega^2 LC)^2 / 2, \quad (10)$$

which can be rewritten in the form

$$P_r = R_s (\omega CV)^2 / [1 - (F/F_{res})^2]^2 / 2, \quad (11)$$

where  $F = 13.56$  MHz is the driving frequency and  $F_{res} = 1/(2\pi\sqrt{LC})$  is the resonance frequency of the equivalent circuit. Using measured parameters discussed in Sec. III E below, we find that for a cell with alumina insulators having  $C = 186$  pF,  $F_{res} = 24$  MHz, and  $R_s = 1 \Omega$ , the dissipation is 2.7 W at  $V = 100$  V. For a cell with PTFE insulators having  $C = 90$  pF,  $F_{res} = 34$  MHz, and  $R_s = 1 \Omega$ , the dissipation is 0.42 W. Since measured powers (see Sec. IV) at  $V = 100$  V typically range from 2 to 15 W, depending on gas pressure, the resistive losses in the shunt can be significant and must be carefully evaluated for accurate determination of discharge power.

## E. Circuit parameters

In order to calculate the electrode voltage and current, values must be determined for the components in the equivalent circuit. The values for  $L$  and  $C$  were determined from measurements of the impedance of the cell at the fundamental frequency and the second harmonic (13.56 and 27.12 MHz) *with the shunt circuit disconnected*. These measurements were made by exciting the empty cell with a low voltage 13.56 MHz square wave or with low voltage sinusoidal signals at these frequencies. Current and voltage were measured with the same probes used for the plasma measurements, and impedance was determined using

$$Z_n = V_n / I_n. \quad (12)$$

The circuit model (Fig. 4 without the shunt circuit) gives the impedance of the empty cell as

$$Z_n = jn\omega L + 1/jn\omega C. \quad (13)$$

$L$  and  $C$  were thus determined by simultaneously solving the equations

$$V_1 / I_1 = j\omega L + 1/j\omega C \quad (14)$$

and

$$V_2 / I_2 = j2\omega L + 1/j2\omega C. \quad (15)$$

Substituting Eqs. (14) and (15) into Eq. (2) shows that when  $L$  and  $C$  are determined in this fashion, values for the fundamental and second harmonic components of the electrode current come out to be identically zero when the cell is empty. Values for the higher harmonic components of the electrode current, calculated from Eq. (2) using the values of  $L$  and  $C$  from Eqs. (14) and (15) and measured values of  $V_n$  and  $I_n$ , are small, but not identically zero. Nonzero values for the magnitudes of the harmonic components occur because the equivalent-circuit model is not exact and because of errors in the measurement probes and the data acquisition process.

The shunt circuit, if used, was then connected and tuned. The shunt capacitance was determined by isolating it and measuring it with a capacitance meter. Finally, the shunt inductance was obtained from the nulling criterion, Eq. (3).

## F. Diagnostic probes

Measurements reported in this article were obtained using a variety of commercially available probes. The selection of a probe by each research group was fairly arbitrary. The various probes, rf power supplies, and matching networks used by each of the research groups are listed in Table I.

Capacitive probes for measuring voltage and inductive probes for measuring current were also developed and served as a reference for comparing to the commercial probes. Construction details and typical parameters for these probes are shown in Fig. 5. These types of probes, which are commonly used in other fields of research,<sup>10,11</sup> are known to have exceptional bandwidth and linearity. If these probes are small and located close together, they

TABLE I. Equipment used for reference cell measurements. (The identification of commercial materials and their sources is made to describe the experiment adequately. In no case does this identification imply recommendation, nor does it imply that the instrument is the best available.)

	NIST <sup>a</sup>	SNL1 <sup>b</sup>	SNL2 <sup>c</sup>	UMI <sup>d</sup>	UNM <sup>e</sup>	WRL <sup>f</sup>
Voltage probe	Philips PM893/109	Tektronix P6015	Capacitive probe	Tektronix P6133	Tektronix P6015	Tektronix P6015
Current probe	Pearson 2878	Pearson 2878	Derivative probe	Pearson 2878	Pearson 2878	Pearson 2877
rf power	rf Plasma Prod. RF5S	ENI ACG-10	ENI ACG-10	ENI ACG-5	Branson/IPC PM122	ENI ACG-10
Matching network	rf Plasma Prod. RF5S	ENI Matchwork 5 <sup>g</sup>	ENI Matchwork 5 <sup>g</sup>	ENI Matchwork 5	rf Plasma Prod. AMN502 <sup>g</sup>	ENI Matchwork 5 <sup>g</sup>
Data acquisition system	Philips PM3323A and PC computer	Tektronix 2430A and PC computer	Tektronix 2430A and PC computer	Tektronix 2430A and PC computer	Tektronix 2430A and PC computer	LeCroy 9400 and HP computer
Mass flow	MKS 1259C	MKS 2258B	MKS 2258B	MKS 2259B	MKS 1259B	Brooks 5850E
Pressure	MKS 390HA	MKS 227	MKS 227	MKS 127A	MKS 122	MKS 127A
High-vacuum pump	Balzers TPU 330	Balzers TPU 330	Balzers TPU 330	Alcatel CFF 450 and Cryogenics/ Cryotorr	Balzers TPU 170	Alcatel 5030 CP

<sup>a</sup>National Institute of Standards and Technology.

<sup>b</sup>Sandia National Laboratories reference cell No. 1.

<sup>c</sup>Sandia National Laboratories reference cell No. 2.

<sup>d</sup>University of Michigan.

<sup>e</sup>University of New Mexico.

<sup>f</sup>Wright Laboratory.

<sup>g</sup>The matching network was replaced by a 0.1  $\mu$ F blocking capacitor when carrying out voltage and current measurements.

provide excellent frequency response and voltage and current information at a common point. The probes do require amplitude calibration at one frequency, which was accomplished by comparing to commercial probes. The signals from the probes are proportional to the derivatives of the

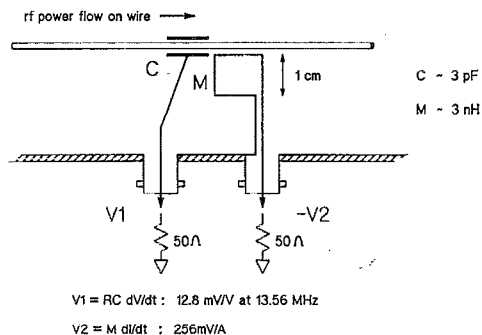


FIG. 5. Schematic diagram of typical derivative probes used to measure voltage and current wave forms. The capacitive voltage probe is a 4-mm inner diameter, 25-mm-long copper tube through which the rf power lead (AWG-#10 insulated wire) passes. Additional insulation is provided by plastic "heat-shrink" tubing between the copper tube and rf power lead. The copper tube is connected by a 2-cm-long wire to a BNC coaxial connector which is mounted on a copper bulkhead. The inductive current probe is a loop of insulated solid copper wire connected to an adjacent BNC connector and arranged as shown. Typical coupling factors and sensitivities are indicated. The probes are held in place by cable ties and adhesive in order to avoid relative mechanical motion which could change calibration factors. Note that the current probe is shown in a mechanically convenient orientation which gives an inverted signal that must be inverted again by the recorder or by software.

voltage and current. This is advantageous because it provides larger signals at the higher frequencies than those that directly measure  $V$  and  $I$  and thus improves the signal-to-noise ratio at the higher harmonics. However, the measured signals must be integrated to obtain the actual voltage and current wave forms. This integration was easily accomplished in the frequency domain, after performing a Fourier transform. (Dividing a signal by  $j\omega$  in the frequency domain is equivalent to integrating that signal in the time domain.)

Since our goal was to measure the amplitudes and phases of the fundamental through the fifth harmonic, it was necessary to determine the accuracy of the voltage and current probes over the frequency range from 13.56 to 67.80 MHz. Furthermore, procedures had to be developed to correct for any significant probe inaccuracies that existed. In general, more difficulties were encountered with phase measurements than with amplitude measurements.

As an example, the results from one set of phase measurements are shown in Fig. 6. Phase errors were determined by driving a purely reactive load (the empty reference cell) whose phase was known over the frequency range of interest (see Sec. IV A). The reactive phase at each driving frequency was measured from voltage and current wave forms using Eq. (12). The measured phase was then compared to the known phase to determine the phase error. There are three curves in Fig. 6. The lowest curve, with the largest phase error, indicates results obtained with a Tektronix P6015 voltage probe and a Pearson

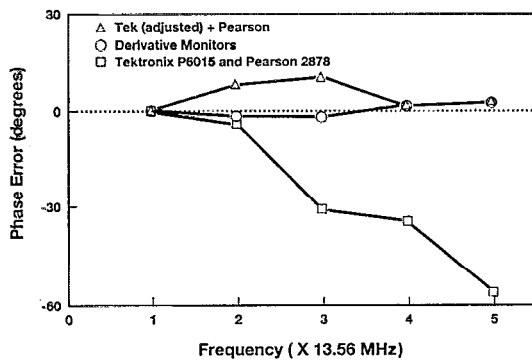


FIG. 6. Representative phase errors in voltage and current probes used with the reference cell. The bottom curve represents the phase error from a pair of commercial probes before adjustment. The derivative-monitor curve represents data from the probes shown in Fig. 6.

2878 current probe as received, without any adjustments. The top curve shows results obtained after the Tektronix probe was adjusted for the best high-frequency amplitude (not phase) response. (The Pearson probe had no adjustments.) The third curve in Fig. 6 shows results from the derivative probes as obtained when the probes were first installed, without adjustment. We conclude that the derivative monitors make good phase references. Regardless of which probe pair was used for measurements, phase corrections were made to the data.

### G. Data acquisition systems

A variety of data acquisition systems were used to obtain and digitize voltage and current wave forms. Systems used to obtain the data in this article are listed in Table I. Most groups used fast Fourier transform (FFT) techniques to convert temporal data to the frequency domain. (The NIST group used a curve-fitting procedure.) Care was taken to insure that the correct amplitudes and phases

were obtained from the routines used to analyze the data. All angles were measured as values between  $-180^\circ$  and  $+180^\circ$  and, by common agreement, the phase of the electrode current fundamental at 13.56 MHz was defined to be zero degrees.

## IV. EXPERIMENTAL RESULTS

### A. Cell parameters

Table II lists values for  $L$ ,  $C$ ,  $L_s$ , and  $C_s$  determined for each reference cell using the procedure outlined in Sec. III E. Equivalent-circuit resonance frequencies ( $F_{res}$ ), insulator materials, base pressures, and leak-up rates (with the cell isolated from all vacuum pumps) are also listed for the various reference cells. Table II also provides information on differences in the way each individual cell was powered. Measurements in all except the WRL cell were made with the bottom electrode powered. Matching networks were only used for measurements made in the NIST and UMI cells; in all other cells the matching network was replaced with a  $0.1 \mu\text{F}$  blocking capacitor. We believe that these differences are representative of those which will be encountered by other research groups making voltage and current measurements in GEC RF reference cells. The degree of agreement between voltage and current measurements should thus be representative of that which other research groups can be expected to achieve.

Two versions of reference cell SNL2 are listed in Table II. Due to early problems in obtaining alumina insulators, one of the cells at Sandia, SNL1, was constructed with alumina insulators while the other, SNL2, was constructed with PTFE insulators. Since the dielectric constant of alumina is roughly twice that of the PTFE, SNL1 had a capacitance value of 193 pF in the equivalent-circuit model, a little more than twice the 84 pF capacitance of SNL2. In order to make the equivalent circuits of the two chambers look as similar as possible, some measurements were made

TABLE II. Reference cell parameters.

Parameter	NIST <sup>a</sup>	SNL1 <sup>b</sup>	SNL2 <sup>c</sup>	SNL2C <sup>d</sup>	UMI <sup>e</sup>	UNM <sup>f</sup>	WRL <sup>g</sup>
$L$ (nH)	125	220	249	229	198	235	256
$C$ (pF)	182	193	84	189	92	95	184
$L_s$ (nH)	1840	1959	1997	1907	...	1868	1590
$C_s$ (pF)	114	94	228	98	...	211	123
$F_{res}$ (MHz) <sup>b</sup>	33	24	34	24	37	34	23
Insulator material <sup>i</sup>	A	A	P	P	P	P	A
Base pressure ( $10^{-5}$ Pa)	0.7	1.1	1.3	1.3	2.9	1.2	0.8
Leak rate (Pa/h)	0.08	0.08	0.07	0.07	1.30	1.30	0.05
Powered electrode <sup>j</sup>	B	B	B	B	B	B	T
Matching network	Yes	No	No	No	Yes	No	No

<sup>a</sup>National Institute of Standards and Technology.

<sup>b</sup>Sandia National Laboratories reference cell No. 1.

<sup>c</sup>Sandia National Laboratories reference cell No. 2.

<sup>d</sup>Sandia National Laboratories reference cell No. 2 with added capacitance.

<sup>e</sup>University of Michigan.

<sup>f</sup>University of New Mexico.

<sup>g</sup>Wright Laboratory.

<sup>h</sup>Calculated from  $F_{res} = 1/(2\pi\sqrt{LC})$ .

<sup>i</sup>A=alumina; P=PTFE.

<sup>j</sup>B=bottom; T=top.



with an external 100 pF capacitor added to SNL2 between the power input lead and ground. With the external capacitor, the cell was referred to as SNL2C (C for capacitor). Assuming that SNL2C could still be modeled with the equivalent circuit of Fig. 4, SNL2C was found to have a capacitance value of 189 pF, in good agreement with the 193 pF measured for SNL1. Comparisons between SNL2C and SNL1 thus provide a good test of our ability to generate similar discharges in chambers with PTFE and alumina insulators. Table II also shows that measurements in the UMI cell were made without the shunt circuit. Comparisons between the UMI cell and other cells with PTFE insulators thus provide a good test of the validity of the shunt circuit.

It is encouraging to note the good agreement between capacitance values for cells with alumina insulators (NIST, SNL1, and WRL) and between cells with PTFE insulators (SNL2, UMI, and UNM); the cells with alumina insulators had capacitance values of  $186 \pm 6$  pF while the cells with PTFE insulators had capacitance values of  $90 \pm 5$  pF. (The capacitance is primarily determined by the dielectric constant of the material between the ground shield and electrode.) An average inductance value of  $231 \pm 21$  nH was measured for all except the NIST cell. The NIST cell had a much lower inductance of 125 nH because  $I$  and  $V$  were measured closer to the driven electrode, resulting in this chamber having an equivalent circuit with a higher resonance frequency than the other chambers with alumina insulators. The small spread in inductance values for the majority of the chambers is indicative of similarities in the placement of the  $I/V$  probes and in the way each individual cell was powered [bottom electrode powered, short (AWG-#10 or larger) power lead length, shunt circuit, etc.]. The calculated resonance frequency of the equivalent circuit can be used to divide the chambers into two groups: those with a resonance at  $24 \pm 1$  MHz (SNL1, SNL2C, and WRL) and those with a resonance at  $34 \pm 2$  MHz (NIST, SNL2, UMI, and UNM). Note that these circuit "resonant" frequencies are not really resonances of the cell because they depend on the physical location of the voltage and current probes, as is readily apparent from the NIST result. The resonant frequency is an important parameter as it determines the reactive phase of the empty chamber. For driving frequencies below  $F_{res}$ , the empty chamber behaves as a capacitive load with a reactive phase of  $-90^\circ$ ; at higher frequencies the chamber behaves as an inductive load with a reactive phase of  $+90^\circ$ .

## B. Measurement reproducibility

Voltage and current measurements made immediately after installation of the individual reference cells showed instabilities and erratic discharge mode changes attributed to uncontrolled surface conditions on the electrodes and discharge chamber walls. Instabilities and mode changes decreased rapidly after the cells were conditioned by running argon discharges for a period of several hours. Data obtained in conditioned cells were reproducible to better than 5% over a period of several months when operating

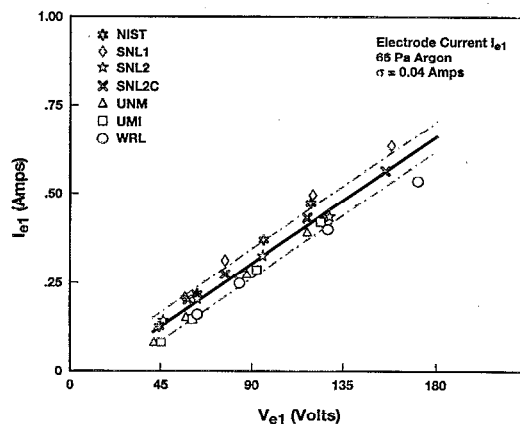


FIG. 7. Representative plot showing the dependence of the electrode current on the electrode voltage. In this and subsequent figures, the solid line is a least squares linear fit to the data and the dot-dash line represents the one-sigma standard deviation ( $\sigma$ ) of the data from the fitted line.

conditions were restricted to argon pressures greater than 13 Pa and peak-to-peak external rf driving voltages less than 250 V. No evidence of hysteresis effects or a dependence on the order in which the data was taken, e.g., high power before low power or vice versa, has been found. Based on extensive experience with the reference cells, deviations from the data presented in Figs. 7 to 13 can be attributed to errors in measurement procedure or to changes in electrode and internal component surface conditioning associated with the use of reactive gases which can modify the internal components of the reference cell. The data presented in Figs. 7 to 13 thus provide a reference which can be used to recover the base line behavior of the reference cell after reactive gases are used, thereby, providing well-characterized initial conditions for the study of reactive gases. Issues associated with discharge uniformity and electron density will be addressed in future reference cell measurements.

## C. Cell behavior at the fundamental driving frequency

We first discuss data comparisons involving the fundamental Fourier components of the voltage and current wave forms as these are least affected by amplitude and phase errors in the voltage and current probes. Measurements were made in argon discharges at a mass flow rate of 20 sccm and pressures of 13, 33, 66, and 133 Pa (i.e., 0.10, 0.25, 0.50, and 1.00 Torr). At each pressure, voltage and current wave forms were measured for peak-to-peak external rf driving voltage of 75, 100, 150, and 200 V. Equations (4)–(6) were used to calculate electrode voltage and current values and Eq. (8) was used to calculate the dissipated power. Phase corrections discussed in Sec. III F were made to each of the measured harmonic components. Due to similarities in the results at each pressure, data is only shown for a representative pressure of 66 Pa. (A complete compilation of all reference cell data is available.<sup>3</sup>)

Figure 7 shows the dependence of the electrode current on the electrode voltage. Due to electrical differences be-

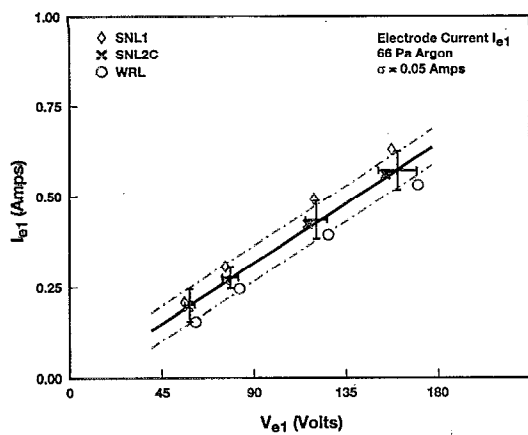


FIG. 8. Representative plot showing the dependence of the electrode current on the electrode voltage in reference cells having equivalent circuits with a resonance at 24 MHz. In this and subsequent figures, points at the intersections of the error bars correspond to mean values of the data at each applied voltage and the lengths of the error bars correspond to standard deviations of the means.

tween the individual cells, the data points corresponding to the four peak-to-peak external rf driving voltages are spread out along a characteristic "operating curve" for the reference cell. The solid line is a least squares linear fit to the data and the dot-dash line represents the one-sigma standard deviation ( $\sigma$ ) of the data from the fitted line. The standard deviation provides a convenient measure of the relative agreement between data sets measured in the different reference cells. The standard deviation of the electrode current increases from 0.02 A at 13 Pa to 0.07 A at 133 Pa. In general, data obtained at 133 Pa show the largest deviation. Because of differences in the slopes of the data sets from each laboratory, the standard deviation does not just reflect an offset of one data set from another. It is encouraging to note that electrode current measurements at the fundamental are uncertain by only  $\pm 5\%$  to  $20\%$

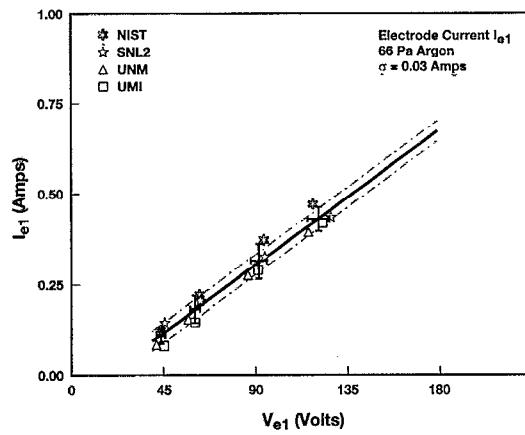


FIG. 9. Representative plot showing the dependence of the electrode current on the electrode voltage in reference cells having equivalent circuits with a resonance at 34 MHz.

even when all the reference cells do not have the same resonance frequency.

It is of interest to investigate the effect of the external driving circuit on the data in Fig. 7. This is conveniently accomplished by using the equivalent-circuit resonance frequency to divide the reference cells into two distinct groups. Results for the three chambers (SNL1, SNL2C, and WRL) with a resonance at 24 MHz and for the four chambers (NIST, SNL2, UMI, and UNM) with a resonance at 34 MHz are shown in Figs. 8 and 9, respectively. Data points in these two figures are seen to cluster into four groups of points corresponding to the four peak-to-peak external rf driving voltages (75, 100, 150, and 200 V). The data clusters indicate good absolute agreement among individual measurements made in cells having equivalent circuits with the same resonance frequency. Mean values and standard deviations of the mean for the magnitude of the electrode-voltage fundamental ( $V_{e1}$ ) and the magnitude of

TABLE III. Electrical properties of reference cells having equivalent circuits with a resonance at 24 MHz.

Pressure (Pa)	$V_{pp}$ (V)	$V_{e1}$ (V)	$\phi_{e1}$ (deg)	$I_{e1}$ (A)	$V_{dc}$ (V)	$P$ (W)
13	75	$57.0 \pm 3.2$	$-70.5 \pm 4.9$	$0.100 \pm 0.001$	$32.8 \pm 1.1$	$0.94 \pm 0.21$
	100	$74.7 \pm 4.7$	$-73.3 \pm 4.8$	$0.132 \pm 0.007$	$48.8 \pm 1.6$	$1.38 \pm 0.35$
	150	$116 \pm 4.0$	$-75.8 \pm 4.6$	$0.193 \pm 0.007$	$87.3 \pm 1.7$	$2.67 \pm 0.73$
	200	$153 \pm 7.0$	$-76.6 \pm 4.7$	$0.242 \pm 0.017$	$123 \pm 4.0$	$4.16 \pm 1.23$
33	75	$57.4 \pm 1.5$	$-70.0 \pm 3.3$	$0.137 \pm 0.033$	$28.6 \pm 6.2$	$1.31 \pm 0.39$
	100	$76.6 \pm 3.0$	$-72.6 \pm 3.2$	$0.185 \pm 0.048$	$44.2 \pm 6.1$	$2.09 \pm 0.51$
	150	$117 \pm 4.0$	$-76.6 \pm 2.6$	$0.344 \pm 0.051$	$81.5 \pm 6.0$	$4.71 \pm 1.24$
	200	$155 \pm 6.0$	$-77.7 \pm 2.5$	$0.443 \pm 0.085$	$116 \pm 4.0$	$7.35 \pm 2.09$
66	75	$59.3 \pm 2.5$	$-70.1 \pm 3.2$	$0.205 \pm 0.044$	$26.3 \pm 4.3$	$2.10 \pm 0.35$
	100	$79.1 \pm 4.1$	$-73.3 \pm 2.4$	$0.279 \pm 0.031$	$44.0 \pm 4.0$	$3.16 \pm 0.70$
	150	$121 \pm 5.0$	$-76.4 \pm 2.3$	$0.443 \pm 0.050$	$81.2 \pm 5.8$	$6.30 \pm 1.70$
	200	$161 \pm 9.0$	$-77.5 \pm 2.1$	$0.582 \pm 0.049$	$116 \pm 4.0$	$9.92 \pm 2.43$
133	75	$60.3 \pm 2.2$	$-69.5 \pm 2.3$	$0.237 \pm 0.052$	$25.8 \pm 5.2$	$2.48 \pm 0.58$
	100	$81.3 \pm 3.7$	$-72.5 \pm 2.2$	$0.353 \pm 0.072$	$42.9 \pm 5.3$	$4.30 \pm 1.02$
	150	$124 \pm 6.0$	$-75.5 \pm 2.1$	$0.593 \pm 0.108$	$79.1 \pm 7.6$	$9.21 \pm 2.70$
	200	$165 \pm 8.0$	$-76.5 \pm 1.9$	$0.824 \pm 0.112$	$113 \pm 11$	$15.6 \pm 3.60$

TABLE IV. Electrical properties of reference cells having equivalent circuits with a resonance at 34 MHz.

Pressure (Pa)	$V_{pp}$ (V)	$V_{e1}$ (V)	$\phi_{e1}$ (deg)	$I_{e1}$ (A)	$V_{dc}$ (V)	$P$ (W)
13	75	44.5 ± 1.6	-71.5 ± 2.0	0.071 ± 0.011	19.0 ± 4.7	0.49 ± 0.07
	100	59.1 ± 1.9	-75.9 ± 1.1	0.100 ± 0.010	30.7 ± 4.9	0.72 ± 0.09
	150	88.8 ± 3.1	-79.7 ± 1.2	0.154 ± 0.012	56.9 ± 8.8	1.22 ± 0.25
	200	119 ± 3.0	-81.8 ± 1.5	0.202 ± 0.014	83.2 ± 11	1.70 ± 0.41
33	75	44.0 ± 2.2	-70.3 ± 2.6	0.093 ± 0.018	15.0 ± 5.8	0.68 ± 0.08
	100	59.4 ± 2.5	-73.9 ± 2.2	0.141 ± 0.021	26.9 ± 6.6	1.15 ± 0.10
	150	89.1 ± 3.7	-77.5 ± 2.5	0.225 ± 0.025	52.6 ± 10	2.16 ± 0.18
	200	121 ± 5.0	-80.3 ± 1.6	0.311 ± 0.026	80.7 ± 14	3.18 ± 0.39
66	75	44.5 ± 1.8	-68.9 ± 3.4	0.108 ± 0.032	11.5 ± 7.5	0.84 ± 0.20
	100	61.2 ± 2.3	-71.9 ± 3.5	0.181 ± 0.037	24.1 ± 9.2	1.68 ± 0.20
	150	92.6 ± 3.9	-76.3 ± 2.7	0.314 ± 0.046	51.8 ± 12	3.40 ± 0.32
	200	122 ± 5.0	-79.2 ± 1.5	0.431 ± 0.035	78.5 ± 13	4.93 ± 0.43
133	75	45.0 ± 2.6	-66.4 ± 4.0	0.137 ± 0.029	11.2 ± 5.1	1.20 ± 0.12
	100	61.2 ± 2.4	-70.7 ± 3.2	0.228 ± 0.033	23.0 ± 6.4	2.28 ± 0.13
	150	93.3 ± 3.4	-75.7 ± 2.2	0.403 ± 0.031	50.3 ± 9.6	4.62 ± 0.32
	200	125 ± 6.0	-76.9 ± 2.6	0.556 ± 0.060	76.3 ± 16	7.78 ± 0.92

the electrode current fundamental ( $I_{e1}$ ) are listed in Tables III and IV for the two sets of cells. The mean value and standard deviation of the mean arc indicated in Figs. 8 and 9 by the points at the intersections of the error bars and the lengths of the error bars, respectively. The sensitivity of the electrode voltage and current data to the external driving circuit is more clearly indicated in Fig. 10 which shows the dependence of the mean electrode voltage on the peak-to-peak external rf driving voltage,  $V_{pp}$ . Figure 10 shows, for example, that the mean electrode voltage corresponding to a fixed 175 V external driving voltage changes almost 50 V when the equivalent-circuit resonance frequency changes from 24 to 34 MHz. Despite this dramatic change, both sets of data lie on the same operating curve as indicated by the solid lines representing least squares linear fits to the data points in Figs. 8 and 9. Standard deviations of the data from the fitted lines are comparable to those in Fig. 7, ranging from 0.01 A at 13 Pa to 0.09 A at 133 Pa for the

data in Fig. 8 and from 0.01 A at 13 Pa to 0.03 A at 133 Pa for the data in Fig. 9.

Mean values and standard deviations of the mean for the dc bias ( $V_{dc}$ ), the phase angle of the electrode-voltage fundamental ( $\phi_{e1}$ ), and the dissipated power ( $P$ ) are also listed in Tables III and IV. Due to similarities to the above results on the electrode current and voltage, plots of the dc bias (Fig. 11), electrode-voltage phase angle (Fig. 12), and dissipated power (Fig. 13) are only shown for the combined data from all reference cells. The apparent anomalous decrease in the electrode-voltage phase angle for electrode voltages greater than 135 V is an artifact which disappears when data from cells with the same resonance frequency are compared. Similarly, the apparent anomalous behavior of the dissipated power in cell SNL1 is an artifact which disappears when data obtained in SNL1 is compared to similar data obtained in cells SNL2C and

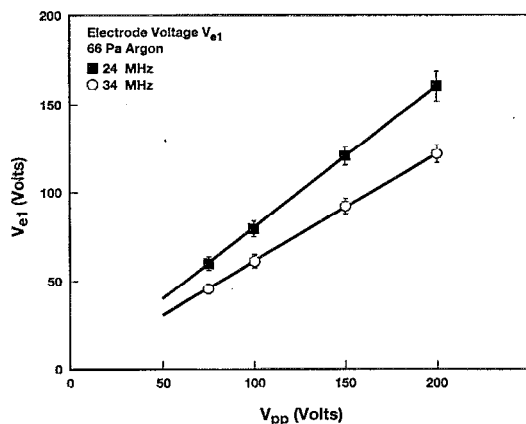


FIG. 10. Representative plot showing the dependence of the electrode voltage on the peak-to-peak rf driving voltage in reference cells with resonances at 24 and 34 MHz.

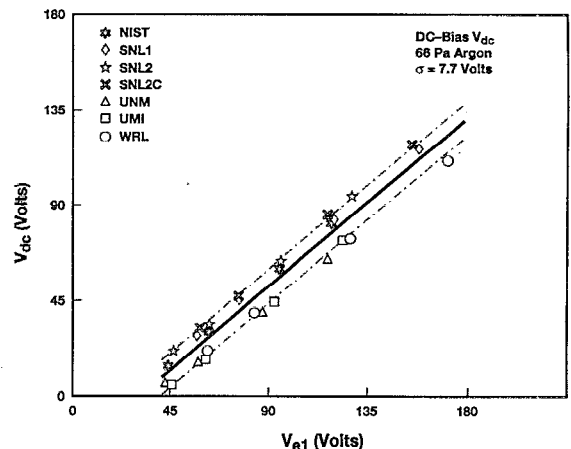


FIG. 11. Representative plot showing the dependence of the dc bias on the electrode voltage.

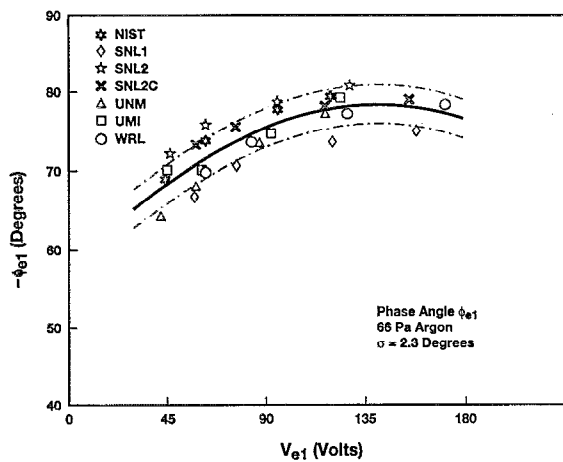


FIG. 12. Representative plot showing the dependence of the electrode-voltage phase angle on the electrode voltage.

WRL with the same equivalent-circuit resonance frequency.

The standard deviations in Tables III and IV indicate excellent agreement was obtained between values used to calculate means for  $V_{e1}$  ( $\% \sigma \sim 4\%$ ),  $\phi_{e1}$  ( $\% \sigma \sim 4\%$ ), and  $I_{e1}$  ( $\% \sigma \sim 14\%$ ). Values used to calculate means for  $V_{dc}$  show a somewhat larger spread with  $\% \sigma$  ranging from  $\sim 9\%$  in cells with a 24 MHz resonance to  $\sim 27\%$  in cells with a 34 MHz resonance. Student's  $t$  test shows that the apparent dependence of  $\% \sigma$  on the resonance frequency of the driving circuit is not statistically significant. The large  $dc$  bias (up to 80% of  $V_{e1}$ ), evident in Tables III and IV and in Fig. 12, reflects the asymmetry in the way each chamber is driven. Percent standard deviations for the dissipated power also show a relatively large spread, ranging from  $\sim 25\%$  in cells with a 24 MHz resonance to  $\sim 13\%$  in cells with a 34 MHz resonance. Again, the difference is not statistically significant. (A possible reason for the increased uncertainty in values for  $V_{dc}$  is discussed in Sec. IV D below.) It should also be noted that  $\% \sigma$  is almost independent of pressure and only shows a weak inverse

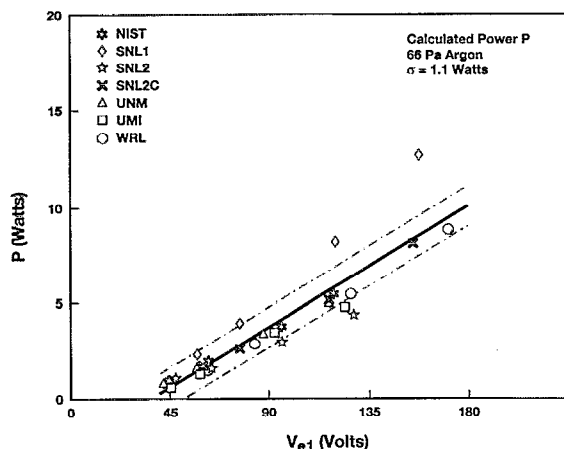


FIG. 13. Representative plot showing the dependence of the dissipated power on the electrode voltage.

dependence on  $V_{pp}$ , with  $\% \sigma$  increasing with decreasing  $V_{pp}$ . All percent standard deviations are consistent with the  $\sim 10\%$  accuracy of the electrical parameters listed in Table I.

The relatively good agreement between measurements made in the UMI cell without the shunt circuit and measurements made in the NIST, SNL2, and UNM cells with the shunt indicates that the shunt circuit does not have a large effect on the fundamental Fourier components of the electrode current and voltage wave forms. Similarly, the good agreement between measurements made in SNL2C and measurements made in SNL1 and WRL indicates that a reference cell with PTFE insulators can be configured to have electrical characteristics with Fourier components at the fundamental driving frequency that are similar to those in cells with alumina insulators.

The classification of the data in Tables III and IV and in Figs. 8–10 according to the resonant frequency of the equivalent circuit is very convenient for these experiments, but can be misleading. Because of the nonlinear nature of the plasma, plasma properties are dependent in unpredictable ways on the impedance over a wide range of frequencies of the circuitry connected to the plasma. The resonant frequency  $F_{res}$  as defined in Eq. (11) above, does not uniquely specify the frequency-dependent impedance seen by the plasma. For example,  $F_{res}$  is a function of the product  $LC$ . Thus two reference cells could have different  $L$  and  $C$  values and yet have identical values of  $F_{res}$ . Furthermore,  $F_{res}$  is a function of the physical location of the voltage and current probes. Consequently, the grouping of the data into two distinct classes corresponding to  $F_{res}$  is partially fortuitous. As shown in Refs. 12 and 13, steps must be taken to match impedances at many frequencies in order to obtain plasmas with the same electrical characteristics at the higher harmonic frequencies.

#### D. Cell behavior at the higher harmonics

The good agreement among the fundamental Fourier components shown in Tables III and IV was not obtained for the higher harmonic components. We expect this, as the higher harmonics are more sensitive to the details of the external circuitry. (See discussion at the end of Sec. IV C above.) To further investigate this, a more detailed comparison was made between the electrical properties of the two reference cells SNL1 and SNL2C at Sandia National Laboratories having equivalent circuits with a resonance at 24 MHz. The external circuits were kept as similar as possible by powering each cell with the same model rf generator using the same length cable and a dc blocking capacitor ( $0.1 \mu F$ ); no matching networks were used. During operation without a matching network, power which is reflected back at the rf generator can affect its operation in ways that depend on the details of its circuitry. However, as long as a particular generator can supply the desired voltage levels without distortion, the reflected power should not affect the characteristics of the discharge. In the present experiments, net power levels were less than 20 W and a generator which can operate with a high voltage-

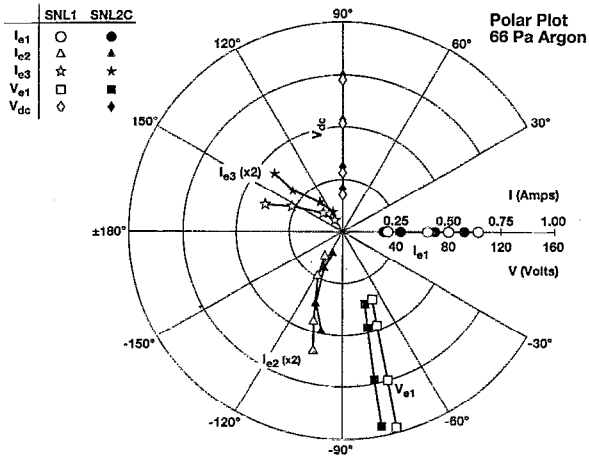


FIG. 14. Representative polar plot showing the electrode voltage, electrode current, and dc bias in reference cells SNL1 and SNL2C. Each cell was powered by the same model rf generator and identical driving circuits. The magnitudes of  $I_{e2}$  and  $I_{e3}$  were multiplied by a factor of 2.

standing-wave ratio (VSWR) was used to power the discharge.

A representative comparison of the data taken in reference cells SNL1 and SNL2C at a pressure of 66 Pa is shown in Fig. 14. The polar plot shows the magnitudes and phases of the first three Fourier coefficients of the electrode current and the magnitude and phase of the electrode-voltage fundamental. The magnitudes of the higher harmonics of the electrode voltage were less than 1% of the fundamental and were thus omitted from the plot. (Comparisons involving the 4th and 5th harmonics were not carried out because of uncertainties in phase and amplitude corrections.) Four connected data points are shown for each parameter, corresponding to the four different peak-to-peak rf voltages applied at the measurement point: 75, 100, 150, and 200 V. In addition, the dc bias was arbitrarily plotted at  $+90^\circ$ . The data in Fig. 14 show less than a 20% discrepancy between the magnitudes and phases of the first three Fourier components of the current. In addition, the dc biases agree to within 5% at all pressures and applied voltages. The magnitudes of the electrode-voltage fundamentals were almost identical, but the absolute values of the voltage phase angles measured in SNL1 were consistently three to seven degrees smaller than those of SNL2C. This discrepancy could be due to the fact that the external circuits of the two cells were not identical because of the additional 100 pF capacitor added to SNL2's external circuit.

Additional comparisons were made between SNL2 and the reference cell at the University of New Mexico. Table II shows that the circuit parameters for these two cells with PTFE insulators (SNL2 and UNM) are within  $\sim 10\%$  of each other. Again, both chambers were powered using identical cables and blocking capacitors, and both cells had shunt circuits with similar values for  $L_s$  and  $C_s$ . Table I shows that the UNM cell was powered with a Branson/IPC model PM122 1000 W rf generator while the

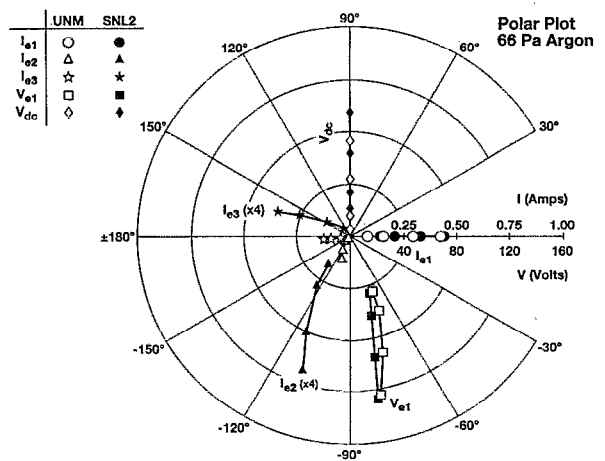


FIG. 15. Representative polar plot showing the electrode voltage, electrode current, and dc bias in reference cells SNL2 and UNM. Each cell was powered by a different type of rf generator but identical driving circuits. The magnitudes of  $I_{e2}$  and  $I_{e3}$  were multiplied by a factor of 4.

SNL2 cell was powered with an ENI ACG-10 600 W rf generator.

A comparison of the data taken in the SNL2 and UNM cells at a pressure of 66 Pa is shown in Fig. 15. The magnitudes and phases of the voltage and current fundamentals are in good agreement (within 15%). However, the UNM cell shows almost no signal at the second or third harmonic of the current. Furthermore, the dc bias of the UNM cell is as much as 50% lower than that of the SNL2 cell. These differences were quite perplexing in view of the effort that had gone into making the two systems look as similar as possible. The only significant difference between the two systems was the rf generators. (It should not be assumed that the rf generators produced sinusoidal driving voltages. Since clipping and other nonlinear voltage wave forms will affect plasma characteristics, care was taken to insure that both generators produced undistorted voltage wave forms.)

The effect of the rf generator was investigated by using the ENI generator from the SNL2 system to power the cell at the University of New Mexico. Data obtained from the SNL2 and UNM cells when they were powered with the same ENI generator are shown in Fig. 16. Again, the magnitudes and phases of the electrode voltage and current fundamentals agreed very well (within 15%). Now, however, the UNM cell also showed significant signals at the second and third harmonics of the current and the dc bias increased. All of the data for these two cells agreed to within 15% at all pressures and applied voltages. This shows dramatically how much the external circuit can affect the harmonics and the dc bias across the discharge. The entire external circuit is important, even the rf generator. The influence of uncontrolled parameters such as the type of rf generator and matching network used with each reference cell may thus explain the relatively large spread in  $\% \sigma$  for the dc bias values listed in Tables III and IV.

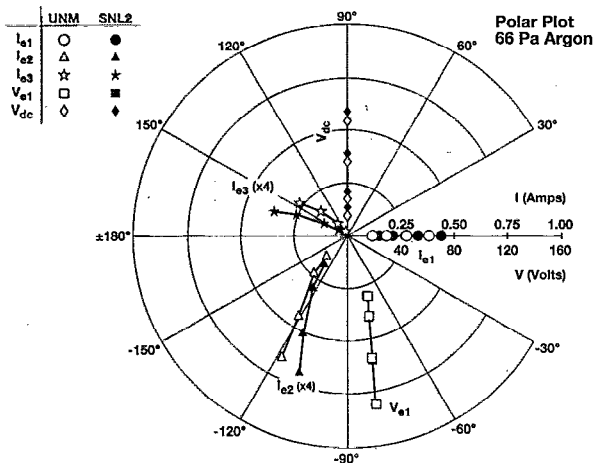


FIG. 16. Representative polar plot showing the electrode voltage, electrode current, and dc bias in reference cells SNL2 and UNM. Each cell was powered with the same rf generator and identical driving circuits. The magnitudes of  $I_{e2}$  and  $I_{e3}$  were multiplied by a factor of 4.

## V. DISCUSSION

Considerable progress has been achieved in obtaining agreement among independent measurements of the electrical properties of GEC RF reference cells at NIST, SNL, UMI, UNM, and WRL through the use of simple additional hardware added to the cell (a stable external shunt circuit) and of an equivalent-circuit model used to obtain current and voltage wave forms at the driven electrode. The simple equivalent circuit in Fig. 4 provides a basis for comparison between cells at the excitation frequency of 13.56 MHz. The level of reproducibility among the five cells contained in this sample set is shown by the data presented in Figs. 7 and 11–13, where one standard deviation limits are indicated by the dashed curves. Over the limited range of operating pressures and applied voltages investigated in this article, values for the amplitude and phase of the fundamental component of the electrode voltage agreed to within  $\sim 4\%$  and values for the amplitude of the fundamental component of the electrode current agreed to within  $\sim 14\%$ . Values for the dc bias voltage and dissipated power showed a somewhat larger spread with the percent standard deviation ranging from  $\sim 10\%$  to  $\sim 25\%$ . Attempts to obtain similar agreement for the higher harmonics were only successful in reference cells with identical external circuit elements. We attribute this to the influence of external circuit elements that were not strictly controlled, e.g., rf power supply and matching network impedance. The good agreement obtained in Fig. 16 between harmonic components of the voltage and current wave forms measured in reference cells with identical rf power sources shows that progress has been made in our phenomenological understanding of the conditions needed to obtain reproducible rf discharges in independent rf reference cells. Methods of isolating the voltage and current measuring point from the external circuit are expected to provide a means to compare higher harmonics among all reference cells independent of the type of rf power source and matching network used to power the cell.<sup>12,13</sup>

The data in Tables III and IV and in Fig. 10 show that for a given applied external voltage, variations in parameters such as the magnitude of the electrode-voltage fundamental and the dc bias can approach 50 V between cells having equivalent circuits with different resonance frequencies. Based on this observation, we recommend that all published voltage and current measurements in rf discharge systems be based on an equivalent-circuit analysis to determine more meaningful “electrode” voltage and current values. However, even use of this technique does not guarantee that “identical” plasma conditions are achieved at higher harmonic frequencies because the plasma responds nonlinearly to the impedance characteristics over a wide frequency range of the external circuitry.

The data in this article clearly show that discharges are strongly affected by the external circuit. The external circuit includes the discharge chamber (or plasma-etching reactor) itself, as well as the other components in the system going from the electrodes to the power supply. All external components including the matching network, cables, and rf supply can affect not only the voltage and current characteristics of the plasma, but also the dc bias. The data taken at the University of New Mexico clearly show that by simply changing the rf generator the dc bias developed across the electrodes can change as much as 30% to 50%. This result has significant implications to commercial plasma-etching reactors. Ostensibly “identical” plasma etchers may operate differently due to subtle, unintentional variations of the external circuits, e.g., length of cables, how the cables are run and attached, internal attachment of power to the electrodes, matching network output impedance, location of matching network, addition of internal and external electrical probes, etc. Furthermore, since these changes can cause large variations of the dc bias, etching processes can be greatly affected as the dc bias largely determines the energy of ions impinging on the wafer. This, then, directly influences the etched profile anisotropy and ion impact assisted surface chemical interactions. Such uncontrolled variations in electrical operating characteristics between reactors make it difficult to transfer a process recipe, knowledge, or insight between installations unless the electrical characteristics of the reactor are completely understood.

## ACKNOWLEDGMENTS

We benefited from numerous suggestions offered by many of the participants at the Gaseous Electronics Conference. We are particularly indebted to Jack Simchock (Sandia) for his contributions to the cell design and to the development of the engineering drawings for the reference cell. Portions of this work performed at Sandia National Laboratories were supported by the U.S. Department of Energy under Contract No. DE-AC04-76DP00789 and by SEMATECH under Contract No. DE-FI04-89AL58872. Work performed at the University of Michigan was supported by National Science Foundation Grant No. CTS-9009899 with equipment support from Semiconductor Research Corporation Contract No. 90-MC-085. Work performed at the University of New Mexico was supported

by SEMATECH under Contract No. 88-MC-502. The work of M. J. Kushner was supported by IBM East Fishkill, the National Science Foundation, and the Semiconductor Research Corporation.

<sup>1</sup>P. J. Hargis, Jr., K. E. Greenberg, P. A. Miller, J. B. Gerardo, R. A. Gottscho, A. Garscadden, P. Bletzinger, J. R. Roberts, J. K. Olthoff, J. R. Whetstone, R. J. Van Brunt, H. M. Anderson, M. L. Passow, M. L. Brake, M. E. Elta, D. B. Graves, M. J. Kushner, J. T. Verdeyen, G. Selwyn, M. Dalvie, J. W. Butterbaugh, H. H. Sawin, T. R. Turner, and R. Horwath, *Bull. Am. Phys. Soc.* **36**, 195 (1990).

<sup>2</sup>K. E. Greenberg, P. J. Hargis, Jr., and P. A. Miller, Sandia National Laboratories Report No. SETEC90-013, 1990.

<sup>3</sup>Send requests to P. J. Hargis, Jr., Sandia National Laboratories, Division 1128, P.O. Box 5800, Albuquerque, New Mexico 87185-0601.

<sup>4</sup>P. A. Miller and M. Kamon, Sandia National Laboratories Report No. SETEC90-009, 1990.

<sup>5</sup>J. R. Roberts, J. K. Olthoff, R. J. Van Brunt, and J. R. Whetstone, *Proc. SPIE* **1392**, 428 (1990); P. A. Miller, *ibid.* **1594**, 179 (1991).

<sup>6</sup>J. T. Verdeyen and P. A. Miller, in *GEC 91, 44th Annual Gaseous*

*Electronics Conference*, 22–25 October, 1991, Albuquerque, New Mexico, Program and Abstracts (University of New Mexico, Albuquerque, 1991), p. 70; M. A. Sobolewski, J. K. Olthoff, J. R. Whetstone, and J. Roberts, *ibid.*, p. 72; J. T. Verdeyen, Sandia National Laboratories Report No. SAND 92-7284, 1992.

<sup>7</sup>J. S. Logan, N. M. Mazza, and P. D. Davide, *J. Vac. Sci. Technol.* **6**, 120 (1969).

<sup>8</sup>A. J. Van Roosmalen, *Appl. Phys. Lett.* **42**, 416 (1983).

<sup>9</sup>J. W. Butterbaugh, L. D. Baston, and H. H. Sawin, *J. Vac. Sci. Technol. A* **8**, 916 (1990).

<sup>10</sup>S. L. Leonard, in *Plasma Diagnostic Techniques*, edited by R. H. Huddleston and S. L. Leonard (Academic, New York, 1965), pp. 7–19.

<sup>11</sup>S. Humphries, Jr., *Principles of Charged Particle Acceleration* (Wiley, New York, 1986), pp. 267–282.

<sup>12</sup>P. A. Miller, H. M. Anderson, and M. P. Splichal, in *GEC 91, 44th Annual Gaseous Electronics Conference*, 22–25 October, 1991, Albuquerque, New Mexico, Program and Abstracts (University of New Mexico, Albuquerque, 1991), p. 69.

<sup>13</sup>P. A. Miller, H. M. Anderson, and M. P. Splichal, *J. Appl. Phys.* **71**, 1171 (1992).